Integer quantum Hall effect and enhanced *g* factor in quantum-confined Cd$_3$As$_2$ films

Run Xiao,[1] Junyi Zhang,[2] Juan Chamorro,[3] Jinwoong Kim,[4] Tyrel M. McQueen,[3]
David Vanderbilt,[4] Morteza Kayyalha,[5] Yi Li,[2] and Nitin Samarth [1,*]

[1]*Department of Physics, The Pennsylvania State University, University Park, Pennsylvania 16802, USA*
[2]*Department of Physics and Astronomy, Institute for Quantum Matter, Johns Hopkins University, Baltimore, Maryland 21218, USA*
[3]*Department of Chemistry, Johns Hopkins University, Baltimore, Maryland 21218, USA*
[4]*Department of Physics and Astronomy, Rutgers University, Piscataway, New Jersey 08854, USA*
[5]*Department of Electrical Engineering, The Pennsylvania State University, University Park, Pennsylvania 16802, USA*

We investigate the integer quantum Hall effect in Cd$_3$As$_2$ thin films under conditions of strong to moderate quantum confinement (thicknesses of 10, 12, and 15 nm). In all the films, we observe the integer quantum Hall effect in the spin-polarized lowest Landau level (filling factor $\nu = 1$) and at spin-degenerate higher index Landau levels with even filling factors ($\nu = 2, 4, 6$). With increasing quantum confinement, we also observe a lifting of the Landau-level spin degeneracy at $\nu = 3$, manifest as the emergence of an anomaly in the longitudinal and Hall resistivities. Tight-binding calculations show that the enhanced *g* factor likely arises from a combination of quantum confinement and corrections from nearby subbands.

Over the past decade, the interplay between strong spin-orbit coupling and crystalline symmetry has created a rich playground for the study of topological phases of quantum matter in materials. Examples include topological insulators [1,2] and topological Dirac and Weyl semimetals [3]. Measurements of quantum transport in such materials yield important insights into the unusual electronic states that host these topological phases [4–11]. In this broad context, the archetypal Dirac semimetal Cd$_3$As$_2$[12,13] with space-group $I4_1/acd$ and two Dirac points on the Γ-Z path protected by inversion, time-reversal symmetry, and C_4 rotational symmetry [14,15] provides a model platform for understanding the underlying topological bulk and surface states (Dirac cones and Fermi arcs, respectively) via measurements of the integer quantum Hall effect (IQHE) [16–24]. In the fully three-dimensional (3D) regime (sample thickness ∼80–150 nm), measurements of the IQHE in Cd$_3$As$_2$ nanoplates have been interpreted in terms of Weyl orbits that involve surface Fermi arcs on opposite surfaces [20,21,25]. The situation becomes more complex in thinner Cd$_3$As$_2$ films (sample thickness ∼10–30 nm). In this regime, quantum confinement is expected to affect the 3D bulk states via a topological phase transition that accompanies the opening of a finite gap between the conduction subbands and the valence subbands. At the same time, the gapless surface states on the top and bottom surfaces of the Cd$_3$As$_2$ thin film can hybridize and open a hybridization gap (as in ultrathin topological insulator films [26]). Thus, understanding the IQHE in this quantum confined regime of Cd$_3$As$_2$ films requires insights into the full interplay between the two-dimensional (2D) quantum confined bulk states [12], the hybridized topological surface states (closed surface Fermi

pockets) [27,28], and surface Fermi arcs [29,30]. Despite concerted efforts to distinguish these various possibilities in experiments [16–19,22–24], a complete understanding of the IQHE in Cd$_3$As$_2$ films in the strongly quantum confined regime (thinner than about 20 nm) remains to be satisfactorily resolved [19,31]. A full first-principles calculation of the Landau levels (LLs) in this regime is also challenging especially for the most commonly studied (112)-oriented Cd$_3$As$_2$ films.

Here, we report on a concerted experimental and theoretical effort to understand the IQHE in Cd$_3$As$_2$ thin films in the limit of strong to moderate quantum confinement (film thickness 10 nm $\leqslant t \leqslant$ 15 nm). We map out the LL spectrum via measurements of the Shubnikov–de Haas (SdH) quantum oscillations and of the fully developed IQHE as a function of chemical potential and magnetic field ($B \leqslant$ 9 T) at low temperature ($T =$ 50 mK). In Cd$_3$As$_2$ films with thicknesses of 15 nm, apart from the $\nu = 1$ quantum Hall plateau, we only observe plateaus at even filling factors $\nu = 2, 4, 6$. This is similar to earlier reports of IQHE in Cd$_3$As$_2$ films of comparable thickness [16,17]. In the thinnest sample that we studied (10-nm thick), we observe the emergence of the $\nu = 3$ quantum Hall state, suggesting that the spin degeneracy has been removed at a relatively modest magnetic field ($B = 9$ T). As an aside, we note that prior quantum transport measurements in very high magnetic fields ($B \geqslant$ 15 T) have shown spin-resolved quantum Hall states with both even and odd filling factors in thicker, quasi-3D Cd$_3$As$_2$ films [17]; this is likely the result of the large *g* factor in bulk Cd$_3$As$_2$ crystals with varying estimated values of $g \sim 16$ [32] and $g \sim 37$ [33]. Our observations are consistent with a new understanding of LLs that emerges from four-band tight-binding model calculations carried out for [112]-oriented quantum confined Cd$_3$As$_2$ films. Our calculations show that quantum confinement results

*Corresponding author: nsamarth@psu.edu

in LLs derived from both bulk subbands and surface states. This produces a nonmonotonic dependence of the g factor on thickness so that an enhanced Zeeman splitting is possible when the film thickness is decreased from 15 to 10 nm. This prediction is consistent with the emergence of a $\nu = 3$ quantum Hall state in the two thinner samples measured in our experiments.

We grew [112]-oriented Cd_3As_2 thin films by molecular beam epitaxy (MBE) in a Veeco EPI 930 chamber using epiready miscut GaAs (111)B substrates [1° toward $(2\bar{1}\bar{1})$]. The epiready GaAs substrates were first annealed inside the MBE chamber to flash off the native oxide at a thermocouple temperature of $820\,°C$ ($T_{\text{actual}} \sim 580\,°C$) whereas monitoring the surface using 12-keV reflection high-energy electron diffraction. Then, we deposited a thin ($\sim$2-nm) GaAs layer at the same substrate temperature to smoothen the surface. Subsequently, the substrates were cooled down to thermocouple temperature of $520\,°C$) under As_4 flux for the growth of a 100-nm GaSb buffer layer with Sb/Ga beam equivalent pressure (BEP) ratio of 7. The substrates were then cooled down further to $400\,°C$ under Sb_4 flux and further cooled down to a thermocouple temperature of $180\,°C$ after closing the Sb shutter. Once the sample temperature was stable at $180\,°C$ ($T_{\text{actual}} \sim 110\,°C$), we evaporated a high-purity Cd_3As_2 compound source from a standard Knudsen effusion cell to deposit a Cd_3As_2 thin film. The desired BEP flux and the growth rate of Cd_3As_2 were controlled by the effusion cell temperature. A BEP flux of around $8\,\mu Pa$ yielded a growth rate of about 0.33 nm/min. During the growth, the pressure of the MBE chamber was maintained at 20 nPa. We used high-resolution cross-sectional transmission electron microscopy to accurately determine the crystalline structure and the thickness (with an uncertainty of ±1 nm) of all films for which we report measurements in this paper [34]. Finally, we also used x-ray diffraction and determined that only peaks from Cd_3As_2 (112) planes are observed. We also note that we have previously used angle-resolved photoemission spectroscopy (ARPES) measurements to show the presence of the expected Dirac semimetal band structure in Cd_3As_2 films grown under similar conditions in the same MBE system [35]. All these characterization measurements confirm that our films have the correct distorted antifluorite phase of Cd_3As_2 for forming a 3D Dirac semimetal.

After the sample growth, we used photolithography and argon plasma etching to pattern the films into two different device geometries: $50\,\mu m \times 25\,\mu m$ Hall bars and $25\,\mu m \times 25\,\mu m$ van der Pauw configurations. We then evaporated 10-nm Ti/30-nm Au as contact electrodes. Finally, we fabricated a top gate composed of a 30-nm Al_2O_3 dielectric layer and 10-nm Ti/30-nm Au contacts, deposited using atomic layer deposition and electron-beam evaporation, respectively. Transport measurements were carried out in a He3/He4 dilution refrigerator (Blue Fors, base temperature $T < 50$ mK, $B \leqslant 9$ T) using lock-in techniques with an excitation current of 1 nA. At base temperature and zero gate voltage, the samples were n type due to the naturally formed As vacancies, with carrier density of about 1×10^{12} cm^{-2} and Drude mobility $\sim 1 \times 10^4$ cm^2 V^{-1} s^{-1}. The application of a voltage to the top gate (V_g) allows the carrier density in the samples to be continuously tuned from n type to p type.

We first discuss the observation of the IQHE in a 15-nm thick Cd_3As_2 film patterned into a van der Pauw geometry device with an electrostatic top gate. The IQHE can be measured either by varying the chemical potential at fixed magnetic field or by varying the magnetic field as fixed gate voltage. In the latter case, the value of the chemical potential changes with the magnetic field to accommodate the increasing degeneracy of LLs. We chose the former approach for convenience. All values of the longitudinal resistivity (ρ_{xx}) and Hall resistivity (ρ_{yx}) that we report have been properly averaged for the van der Pauw configuration. The magnetic field B is always applied perpendicular to the plane of the sample. Figure 1(a) shows the variation of ρ_{xx} as a function of V_g at zero magnetic field. At $V_g = 0$ V, the sample is n type (see the details in the Supplemental Material [34]). Applying a negative gate voltage moves the chemical potential toward the valence band, and ρ_{xx} rises to a peak value of 4.2 kΩ at the charge neutral point (CNP) at $V_g = V_G^{CNP} = -2$ V. Applying a positive gate voltage shifts the chemical potential higher up into the conduction band and reduces ρ_{xx} from its value at zero gate voltage. Figure 1(b) shows the variation of ρ_{xx} and ρ_{yx} with V_g at a fixed field magnitude $B = 9$ T. We see clear evidence of the IQHE wherein Hall plateaus ($\rho_{yx} = \frac{h}{\nu e^2}$) are accompanied by $\rho_{xx} \sim 0$. By using the standard conversion of ρ_{xx} into a Hall conductivity σ_{xy}, we find that the filling factors associated with these plateaus are $\nu = 1, 2, 4, 6$ [Fig. 1(c)]. For the quantum Hall plateaus with $\nu = 1, 2, 4$ in Fig. 1(b), ρ_{xx} has values 203.6, 0.92, 0.33 Ω, and ρ_{yx} has values 0.997, 0.4967, and 0.2472 h/e^2, respectively. It is interesting to note that the $\nu = 1$ quantum Hall state is not as robust as $\nu = 2$: the plateau is not as wide in the former as it is in the latter and the minimum in ρ_{xx} is also not as deep. This indicates that the gap at $\nu = 1$ is smaller than that associated with $\nu = 2$. This resembles the behavior seen in single layer and bilayer graphene.

Since the IQHE is not well developed at large filling factors ($\nu > 6$), we determine the filling factors using the derivative of ρ_{xx}. First, Hall plateaus and quantum oscillations corresponding to higher filling factors are easier to determine in the derivative of ρ_{xx} (see Fig. S1 in the Supplemental Material [34]). This yields even filling factors $\nu = 8, 10$. Next, we construct a LL fan diagram by plotting ρ_{xx} as a function of B and V_g. Figure 1(d) shows such a plot for a given orientation of magnetic field. The plot is generated by sweeping V_g at fixed magnetic field and the quantity plotted is $R_{14,23}$ wherein current is passed between terminals 1,2 and voltage is measured across terminals 3,4 [see inset in Fig. 1(a)]. The linear-in-field features in the LL fan can be assigned to filling factors $\nu = 1, 2, 4, 6, 8, 10, 12$ (see Fig. S2 of the Supplemental Material [34]). We, thus, conclude that the IQHE in 15-nm Cd_3As_2 thin films only occurs at $\nu = 1$ and at higher even filling factors; this is consistent with previous studies of Cd_3As_2 thin films of similar thickness ($t \sim 10$–20 nm) [16–18]. However, as we show below, our measurements of the IQHE in the 10-nm Cd_3As_2 film reveal a new feature not seen in previous reports.

Figure 2 shows the transport properties of a 10-nm thick Cd_3As_2 thin film at 50 mK. At $B = 0$ T, ρ_{xx} dramatically increases when the chemical potential is tuned to the CNP with the resistance of the sample going beyond the range of
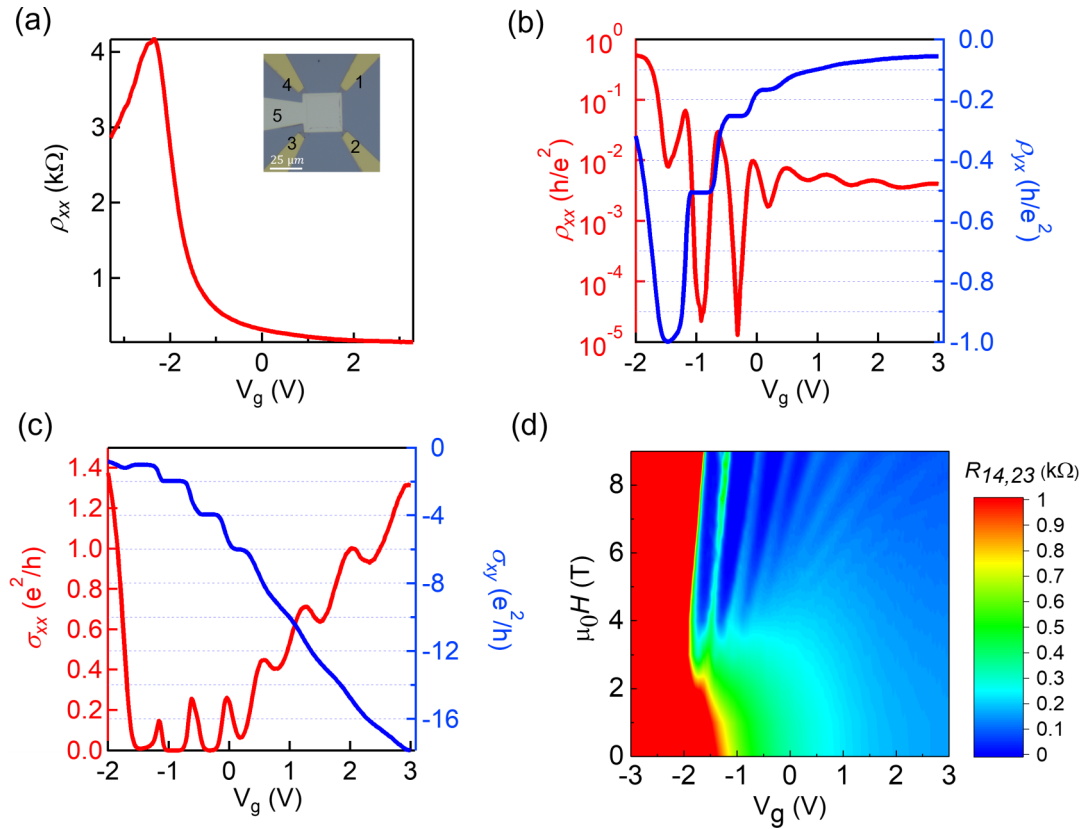
FIG. 1. IQHE in a moderately quantum confined 15-nm-thick Cd_3As_2 film at $T = 50$ mK. (a) Gate-voltage dependence of ρ_{xx} at zero magnetic field. The inset shows a schematic of the Van der Pauw geometry. (b) Gate voltage dependence of ρ_{xx} (red, left axis) and ρ_{yx} (blue, right axis) at $B = 9$ T, showing quantized Hall plateaus at filling factor $\nu = 1, 2, 4, 6$ accompanied by deep minima in ρ_{xx}. The finite minimum at $\nu = 1$ ($\rho_{xx} \sim 200\ \Omega$) is attributed to the incomplete development of the first LL at $B = 9$ T. (c) Gate voltage dependence of σ_{xx} (red, left axis) and σ_{xx} (blue, right axis) at $B = 9$ T. These values are obtained from the data in (b). (d) Variation of $R_{14,23}$ with B and V_g, where $R_{14,23} = V_{23}/I_{14}$. The plot is generated by sweeping V_g at fixed values of B. The magnetic field is incremented in steps of 0.2 T for $B \geqslant 4$ T and in steps of 1 T for $B < 4$ T. The data are then smoothly interpolated. A raw plot is provided in the Supplemental Material [34].

the lock-in amplifier, showing a completely insulating behavior. At $B = 9$ T, when the chemical potential is tuned away from the CNP, the sample exhibits the IQHE, similar to the 15-nm-thick film, with quantum Hall plateaus corresponding to $\nu = 1, 2, 4, 6, 8$ [Figs. 2(b) and 2(c)]. In addition, we observe the signature of the $\nu = 3$ quantum Hall state by fine tuning V_g. This is seen more clearly in the first derivative plots of ρ_{xx} and ρ_{yx} with respect to V_g when $V_g \approx 0.06$ V [Fig. 2(d)]. In Figs. 3(a)–3(c), we compare the evolution of the signature of the $\nu = 3$ quantum Hall state with different thicknesses. Note that there is no sign of the $\nu = 3$ state in the 15-nm-thick film; this only becomes more obvious as the quantum confinement becomes stronger in the two thinner films.

We now seek a theoretical understanding of the quantum confinement effects on the band structure and how the modifications in band structure affect the LLs and the g factor in ultrathin Cd_3As_2 films. The quantum confinement gives rise to quasi-2D subbands derived from 3D electronic states. As the bulk Dirac points located at $\mathbf{k}_D^{\pm} = \pm(0, 0, k_D)$ are projected to the (112) surface Brillouin zone (SBZ) to two separate points, $\bar{\mathbf{k}}_D^+$ and $\bar{\mathbf{k}}_D^-$, surface (or surfacelike) states are supported in (112)-oriented films. Figure 3(d) shows the projected bulk

bands (blue) and the surface states (red) for a 280-nm-thick film, calculated using a four-band tight-binding model [36] (see also Sec. V in the Supplemental Material [34]). The existence of surface states has also been confirmed by ARPES experiments in bulk crystals [37,38] and more recently in 30-nm thin films [35]. In thick films, the surface Dirac node at $\bar{\Gamma}$ (the projection of the Γ point in the SBZ) is topologically protected, whereas the dispersion of the surface states depends on many factors, such as the confinement potential, nature of the substrate and the termination layer. As chemical potential varies, a ring-shaped closed Fermi arc around $\bar{\Gamma}$ or a pair of open Fermi arcs bridging $\bar{\mathbf{k}}_D^+$ and $\bar{\mathbf{k}}_D^-$ can be supported. The topology of the surface Fermi arcs changes at a surface Lifshitz transition [36].

In thin films, quantum confinement strongly modifies the band structure. It splits bulk bands into quasi-2D subbands and can further hybridize topological gapless surface states discussed above to form gapped surfacelike bands. As shown in Fig. 3(e), for the tight-binding model band structure of a (112)-oriented Cd_3As_2 film with thickness $t \sim 13$ nm, as an example, the energy separation between the subbands near $\bar{\mathbf{k}}_D^{\pm}$ is on the order of 30 meV. This is consistent with the confinement splitting $\Delta E = \hbar \pi v / t$ where $\hbar v \sim 0.1$ eV nm near $\mathbf{k}_D^{\pm}$
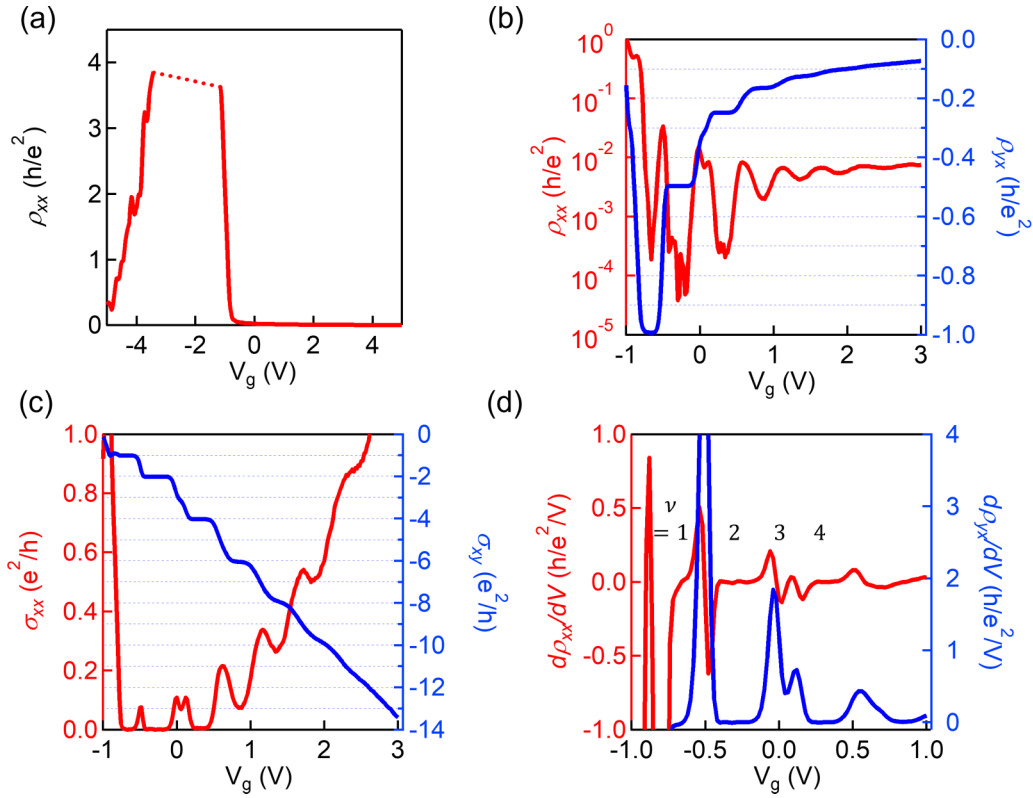
FIG. 2. IQHE in a strongly quantum confined 10-nm-thick Cd_3As_2 thin film at $T = 50$ mK. (a) Variation of σ_{xx} with V_g at $B = 0$. When the chemical potential is close to the CNP, we cannot reliably measure σ_{xx} using lock-in techniques (represented by the dashed line). (b) V_g dependence of σ_{xx} (red, left axis) and σ_{xy}(blue, right axis) at $B = 9$ T. For the $\nu = 1, 2, 4$ quantum Hall plateaus, ρ_{xx} has values of 4.8, 0.98, 5.9 Ω, whereas ρ_{yx} has values of 0.9937, 0.4973, and 0.2483 h/e^2, respectively. (c) V_g dependence of σ_{xx} (red, left axis) and σ_{xy} (blue, right axis) at $B = 9$ T. These values are obtained from the data in (b). (d) The first derivative plot of the data in (b), showing the quantum Hall states with filling factor $\nu = 1$–4.

[15]. In addition to the confinement splitting, Fig. 3(e) shows a smaller gap, $\Delta_{hyb} \sim 2.3$ meV, between the lowest conduction subband c_1, and the highest valence subband v_1, near $\bar{\Gamma}$. Comparing with Fig. 3(d), we can see that the dispersions of c_1 and v_1 near $\bar{\Gamma}$ are modified slightly from those of the surface states in the thicker film. Furthermore, Δ_{hyb} increases for thinner films, so Δ_{hyb} arises from the hybridization of surface states.

Since the IQHE is observed in ultrathin films of Cd_3As_2 with low n-doped carrier concentrations, we focus on the contribution from the lowest conduction subband c_1. As c_1 hybridizes with the highest valence subband v_1 near $\bar{\Gamma}$, these two bands together can be described by an anisotropic 2D massive Dirac Hamiltonian,

$$H_{MD} = \Delta_{hyb}\sigma_z + v_\xi \Pi_\xi \sigma_x + v_\eta \Pi_\eta \sigma_y, \quad (1)$$

under a magnetic field along [112], where v_i and $\Pi_i = p_i + eA_i$ are, respectively, the Dirac velocity and kinetic momentum along the ith direction on the (112) plane with $i = \xi$ and η [39].

We solve the LL energies of the above anisotropic massive Dirac subbands as [34]

$$E_{LL}^{n_L} = \sqrt{\Delta^2 + (n_L + \gamma)(2\hbar eB_\zeta v_\xi v_\eta)} + \frac{1}{2}g_{\text{eff},\zeta}\mu_B B_\zeta,$$
$$n \geqslant 0, \quad (2)$$

where γ accounts for the effect of the Berry phase of the subbands and B_ζ represents the Zeeman shift. B_ζ is the magnitude of the magnetic field along [112]. $g_{\text{eff},\zeta} = g_0 + 2g'$ consists of the usual spin Zeeman effect and the anomalous correction from orbital motion.

Since the g factor of topological surface states near the bottom of the lowest conduction subband is larger than that of higher LLs, the degeneracy of the first LL is lifted due to spin splitting. As a result, both the $\nu = 1$ and the $\nu = 2$ quantum Hall plateaus can be observed in Cd_3As_2 films of all thicknesses studied in our experiments.

Next, we discuss the emergence of the $\nu = 3$ quantum Hall state which indicates an anomalous enhancement of the g factor with decreasing film thickness. To understand the thickness dependence of the g factor, we consider two quantum confinement contributions to the g factor as follows. First, as the film thickness decreases, the confinement energy splitting between quasi-2D subbands increases. As a result, the magnitude of the correction to the g factor, which is inversely proportional to the energy gap between subbands, decreases. This has been observed in Cd_3As_2 films with thickness varying from 12 to 100 nm in, for example, Ref. [17], where the substrate and the doping level are different from our system. Second, for an ultrathin film of a topological material, hybridized bands with surfacelike states near the chemical potential can play an important role in transport. Since these
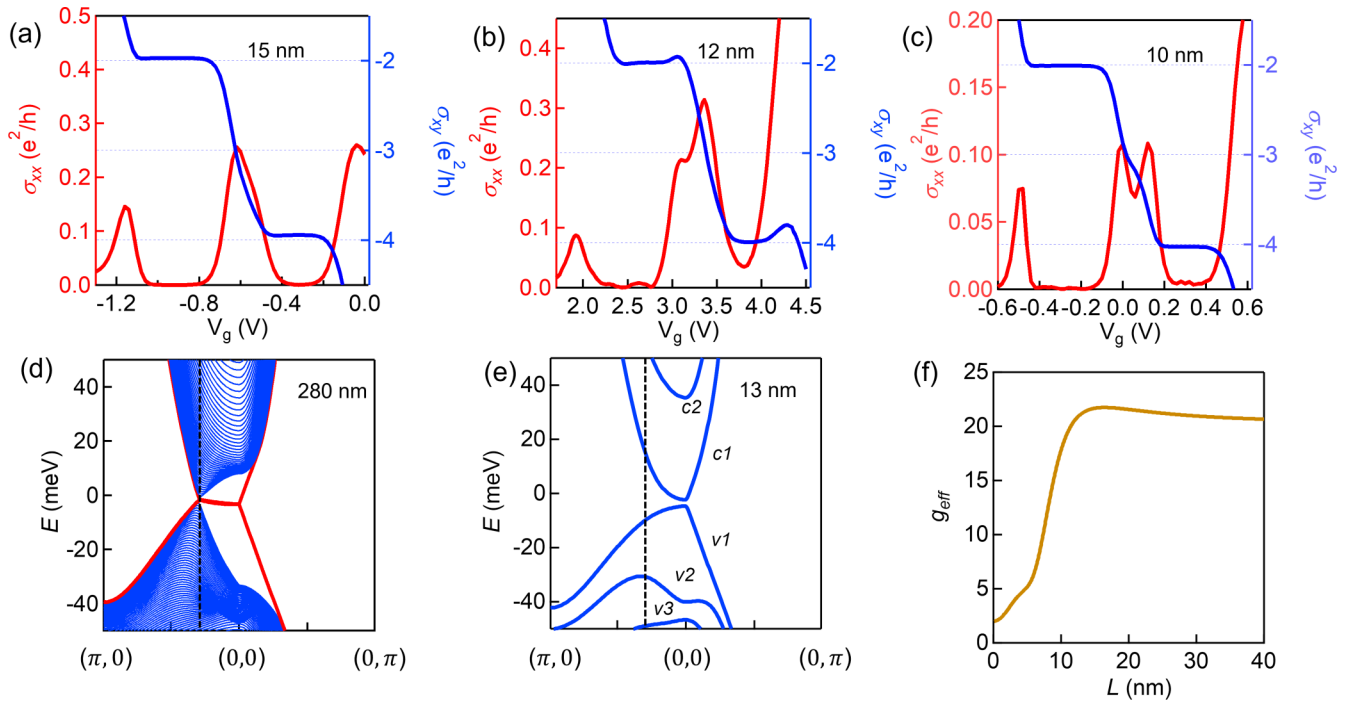
FIG. 3. (a)–(c) Experimentally measured evolution of the $\nu = 3$ feature in Cd_3As_2 films with different thickness: (a) 15, (b) 12, and (c) 10 nm. Each panel shows the V_g dependence of σ_{xx} (red, left axis) and σ_{xy} (blue, right axis) at $B = 9$ T. (d) and (e) Band structure in the surface Brillouin zone of [112]-oriented films, based on a tight-binding model of two different thicknesses: (d) 280 nm (e) 13 nm. The vertical dashed line indicates the projection of the bulk Dirac point $\mathbf{k}_D^+$ in the SBZ at $(0.3\pi, 0)$. Blue and red indicate bulk and surface states, respectively, in panel (d). The calculation shows a quantum confinement induced band gap of 2.3 meV in the thinner case. (f) Calculated g factors as a function of Cd_3As_2 film thickness.

surfacelike states break parity, they carry symmetry lower than that of the bulk bands. Consequently, more subbands are allowed by symmetry to contribute to the perturbation correction of the g factor based on Roth's formula [40,41]. Furthermore, for our thin films of Cd_3As_2, the energy of the valence subband closest to the hybridized massive Dirac bands, v_2 in Fig. 3(e), can exhibit a nonmonotonic thickness dependence. (This can be inferred from nonmonotonic dispersion of the Γ_6^- bulk band along Γ-Z in Refs. [12,15].) Therefore, the g factor can inherit a complicated thickness dependence on the energy gaps between hybridized bands at chemical potential and other nearby subbands. A detailed derivation of the g factor for the (112) Cd_3As_2 thin film is provided in Sec. VII of the Supplemental Material [34].

As shown in Fig. 3(f), in thick films, g_{eff} approaches its large value (~ 20) in the bulk. When the films get thinner than 10 nm, g_{eff} quickly quenches with a knee to a value of about 5 at the thickness of 5 nm. However, when the thickness is between 10 and 15 nm, the dependence of g_{eff} on thickness is nonmonotonic. This feature is consistent with our experimental observation of a signature of the $\nu = 3$ state in the 10-nm-thick film. In addition, besides the correction from the nearby subbands, these features (knee, quench, and slight rising) are highly dependent on the specific band dispersion which can be affected by details of the hybridization, the confinement potential, and the substrate. These effects, especially the influence of the substrate, likely play an important role in the differences between our data and that in a

previous report which used Cd_3As_2 films grown on a different substrate [17].

To summarize, we have mapped out the behavior of SdH oscillations and the IQHE in quantum confined Cd_3As_2 thin films as a function of magnetic field and chemical potential. When the chemical potential is above the CNP, we observe clear quantum oscillations and quantum Hall plateaus at magnetic fields larger than 4 T. Under these conditions, quantum Hall states with filling factors $\nu = 1, 2, 4, 6$ are well developed in 10- to 15-nm-thick films. As the film thickness approaches 10 nm, a signature of the $\nu = 3$ quantum Hall state begins to emerge due to an enhancement of the g factor (and, thus, larger Zeeman splitting). Tight-binding calculations show that quantum confinement is likely responsible for this enhanced g factor. The g factor in ultrathin films may also be larger due to the correction from nearby subbands. These new insights change earlier expectations that the g factor in Cd_3As_2 would become monotonically smaller as the film thickness decreases. The combination of experiment and theory used in this Letter gives us a comprehensive understanding of the band structure and the thickness dependence of the g factor in Cd_3As_2 thin films under quantum confinement. We anticipate that our results will motivate more thorough studies of the IQHE in strongly quantum confined topological semimetal thin films.

[1] M. Z. Hasan and C. L. Kane, Colloquium: Topological insulators, Rev. Mod. Phys. **82**, 3045 (2010).

[2] X.-L. Qi and S.-C. Zhang, Topological insulators and superconductors, Rev. Mod. Phys. **83**, 1057 (2011).

[3] N. P. Armitage, E. J. Mele, and A. Vishwanath, Weyl and Dirac semimetals in three-dimensional solids, Rev. Mod. Phys. **90**, 015001 (2018).

[4] M. König, S. Wiedmann, C. Brune, A. Roth, H. Buhmann, L. W. Molenkamp, X.-L. Qi, and S.-C. Zhang, Quantum spin Hall insulator state in HgTe quantum wells Science **318**, 766 (2007).

[5] C.-Z. Chang, J. Zhang, X. Feng, J. Shen, Z. Zhang, M. Guo, K. Li, Y. Ou, P. Wei, L.-L. Wang, Z.-Q. Ji, Y. Feng, S. Ji, X. Chen, J. Jia, X. Dai, Z. Fang, S.-C. Zhang, K. He, Y. Wang *et al.*, Experimental observation of the quantum anomalous Hall effect in a magnetic topological insulator, Science **340**, 167 (2013).

[6] T. Liang, Q. Gibson, M. N. Ali, M. Liu, R. Cava, and N. Ong, Ultrahigh mobility and giant magnetoresistance in the Dirac semimetal Cd_3As_2, Nature Mater. **14**, 280 (2015).

[7] J. Xiong, S. K. Kushwaha, T. Liang, J. W. Krizan, M. Hirschberger, W. Wang, R. J. Cava, and N. P. Ong, Evidence for the chiral anomaly in the Dirac semimetal Na_3Bi, Science **350**, 413 (2015).

[8] X. Huang, L. Zhao, Y. Long, P. Wang, D. Chen, Z. Yang, H. Liang, M. Xue, H. Weng, Z. Fang, X. Dai, and G. Chen, Observation of the Chiral-Anomaly-Induced Negative Magnetoresistance in 3D Weyl Semimetal TaAs, Phys. Rev. X **5**, 031023 (2015).

[9] S. Liang, J. Lin, S. Kushwaha, J. Xing, N. Ni, R. J. Cava, and N. P. Ong, Experimental tests of the chiral anomaly magnetoresistance in the Dirac-Weyl semimetals Na_3Bi and GdPtBi, Phys. Rev. X **8**, 031002 (2018).

[10] N. Ong and S. Liang, Experimental signatures of the chiral anomaly in Dirac-Weyl semimetals, Nat. Rev. Phys. **3**, 394 (2021).

[11] B. A. Bernevig, C. Felser, and H. Beidenkopf, Progress and prospects in magnetic topological materials, Nature (London) **603**, 41 (2022).

[12] Z. Wang, H. Weng, Q. Wu, X. Dai, and Z. Fang, Three-dimensional Dirac semimetal and quantum transport in Cd_3As_2, Phys. Rev. B **88**, 125427 (2013).

[13] Z. K. Liu, B. Zhou, Y. Zhang, Z. J. Wang, H. M. Weng, D. Prabhakaran, S.-K. Mo, Z. X. Shen, Z. Fang, X. Dai, Z. Hussain, and Y. L. Chen, Discovery of a three-dimensional topological Dirac semimetal, Na_3Bi, Science **343**, 864 (2014).

[14] M. N. Ali, Q. Gibson, S. Jeon, B. B. Zhou, A. Yazdani, and R. J. Cava, The crystal and electronic structures of Cd_3As_2, the three-dimensional electronic analogue of graphene, Inorg. Chem. **53**, 4062 (2014).

[15] S. Baidya and D. Vanderbilt, First-principles theory of the Dirac semimetal Cd_3As_2 under Zeeman magnetic field, Phys. Rev. B **102**, 165115 (2020).

[16] T. Schumann, L. Galletti, D. A. Kealhofer, H. Kim, M. Goyal, and S. Stemmer, Observation of the Quantum Hall Effect in Confined Films of the Three-Dimensional Dirac Semimetal Cd_3As_2, Phys. Rev. Lett. **120**, 016801 (2018).

[17] M. Uchida, Y. Nakazawa, S. Nishihaya, K. Akiba, M. Kriener, Y. Kozuka, A. Miyake, Y. Taguchi, M. Tokunaga, N. Nagaosa, Y. Tokura, and M. Kawasaki, Quantum Hall states observed in thin films of Dirac semimetal Cd_3As_2, Nat. Commun. **8**, 2274 (2017).

[18] M. Goyal, L. Galletti, S. Salmani-Rezaie, T. Schumann, D. A. Kealhofer, and S. Stemmer, Thickness dependence of the quantum Hall effect in films of the three-dimensional Dirac semimetal Cd_3As_2, APL Mater. **6**, 026105 (2018).

[19] L. Galletti, T. Schumann, D. A. Kealhofer, M. Goyal, and S. Stemmer, Absence of signatures of Weyl orbits in the thickness dependence of quantum transport in cadmium arsenide, Phys. Rev. B **99**, 201401(R) (2019).

[20] C. Zhang, Y. Zhang, X. Yuan, S. Lu, J. Zhang, A. Narayan, Y. Liu, H. Zhang, Z. Ni, R. Liu, E. S. Choi, A. Suslov, S. Sanvito, L. Pi, H.-Z. Lu, A. C. Potter, and F. Xiu, Quantum Hall effect based on Weyl orbits in Cd_3As_2, Nature (London) **565**, 331 (2019).

[21] C. Zhang, A. Narayan, S. Lu, J. Zhang, H. Zhang, Z. Ni, X. Yuan, Y. Liu, J.-H. Park, E. Zhang, W. Wang, S. Liu, L. Cheng, L. Pi, Z. Sheng, S. Sanvito, and F. Xiu, Evolution of Weyl orbit and quantum Hall effect in Dirac semimetal Cd_3As_2, Nat. Commun. **8**, 1272 (2017).

[22] S. Nishihaya, M. Uchida, Y. Nakazawa, M. Kriener, Y. Kozuka, Y. Taguchi, and M. Kawasaki, Gate-tuned quantum Hall states in Dirac semimetal $(Cd_{1-x}Zn_x)_3As_2$, Sci. Adv. **4**, eaar5668 (2018).

[23] S. Nishihaya, M. Uchida, Y. Nakazawa, R. Kurihara, K. Akiba, M. Kriener, A. Miyake, Y. Taguchi, M. Tokunaga, and M. Kawasaki, Quantized surface transport in topological Dirac semimetal films, Nat. Commun. **10**, 2564 (2019).

[24] S. Nishihaya, M. Uchida, Y. Nakazawa, M. Kriener, Y. Taguchi, and M. Kawasaki, Intrinsic coupling between spatially-separated surface Fermi-arcs in Weyl orbit quantum Hall states, Nat. Commun. **12**, 2572 (2021).

[25] H. Li, H. Liu, H. Jiang, and X. C. Xie, 3D Quantum Hall Effect and a Global Picture of Edge States in Weyl Semimetals, Phys. Rev. Lett. **125**, 036602 (2020).

[26] C.-X. Liu, H. Zhang, B. Yan, X.-L. Qi, T. Frauenheim, X. Dai, Z. Fang, and S.-C. Zhang, Oscillatory crossover from two-dimensional to three-dimensional topological insulators, Phys. Rev. B **81**, 041307(R) (2010).

[27] M. Kargarian, M. Randeria, and Y.-M. Lu, Are the surface Fermi arcs in Dirac semimetals topologically protected? Proc. Natl. Acad. Sci. U.S.A. **113**, 8648 (2016).

[28] J. W. Villanova, E. Barnes, and K. Park, Engineering and probing topological properties of Dirac semimetal films by asymmetric charge transfer, Nano Lett. **17**, 963 (2017).

[29] P. V. Arribi, J.-X. Zhu, T. Schumann, S. Stemmer, A. A. Burkov, and O. Heinonen, Topological surface states in strained Dirac semimetal thin films, Phys. Rev. B **102**, 155141 (2020).

[30] A. C. Potter, I. Kimchi, and A. Vishwanath, Quantum oscillations from surface Fermi arcs in Weyl and Dirac semimetals, Nat. Commun. **5**, 5161 (2014).

[31] R. Chen, C. M. Wang, T. Liu, H.-Z. Lu, and X. C. Xie, Quantum Hall effect originated from helical edge states in Cd_3As_2, Phys. Rev. Res. **3**, 033227 (2021).

[32] A. Narayanan, M. D. Watson, S. F. Blake, N. Bruyant, L. Drigo, Y. L. Chen, D. Prabhakaran, B. Yan, C. Felser, T. Kong, P. C. Canfield, and A. I. Coldea, Linear Magnetoresistance Caused by Mobility Fluctuations in *n*-doped Cd_3As_2, Phys. Rev. Lett. **114**, 117201 (2015).

[33] S. Jeon, B. B. Zhou, A. Gyenis, B. E. Feldman, I. Kimchi, A. C. Potter, Q. D. Gibson, R. J. Cava, A. Vishwanath, and A. Yazdani, Landau quantization and quasiparticle interference in

the three-dimensional Dirac semimetal Cd_3As_2, Nature Mater. **13**, 851 (2014).

[34] See Supplemental Material at http://link.aps.org/supplemental/ 10.1103/PhysRevB.106.L201101 for additional TEM and transport data.

[35] W. Yanez, Y. Ou, R. Xiao, J. Koo, J. T. Held, S. Ghosh, J. Rable, T. Pillsbury, E. G. Delgado, K. Yang, J. Chamorro, A. J. Grutter, P. Quarterman, A. Richardella, A. Sengupta, T. McQueen, J. A. Borchers, K. A. Mkhoyan, B. Yan, and N. Samarth, Spin and Charge Interconversion in Dirac-Semimetal Thin Films, Phys. Rev. Appl. **16**, 054031 (2021).

[36] J. Zhang, J. Kim, D. Vanderbilt, and Y. Li, Mobius Weyl orbits and magnetic-field-induced topological phase transitions in Dirac semimetal films (unpublished).

[37] H. Yi, Z. Wang, C. Chen, Y. Shi, Y. Feng, A. Liang, Z. Xie, S. He, J. He, Y. Peng, X. Liu, Y. Liu, L. Zhao, G. Liu, X. Dong, J. Zhang, M. Nakatake, M. Arita, K. Shimada, H. Namatame, M.

Taniguchi, Z. Xu, C. Chen, X. Dai, Z. Fang, and X. J. Zhou, Evidence of topological surface state in three-dimensional Dirac semimetal Cd_3As_2, Sci. Rep. **4**, 6106 (2014).

[38] S. Roth, H. Lee, A. Sterzi, M. Zacchigna, A. Politano, R. Sankar, F. C. Chou, G. Di Santo, L. Petaccia, O. V. Yazyev, and A. Crepaldi, Reinvestigating the surface and bulk electronic properties of Cd_3As_2, Phys. Rev. B **97**, 165439 (2018).

[39] The in-plane ξ axis is along the projection of the c axis and the in-plane η axis is perpendicular to the ξ axis. In SBZ, the $(\pi, 0)$ direction $(0, \pi)$, respectively]is along the ξ axis (η axis, resprctively).

[40] L. M. Roth, B. Lax, and S. Zwerdling, Theory of optical magneto-absorption effects in semiconductors, Phys. Rev. **114**, 90 (1959).

[41] R. Winkler, *Spin-Orbit Coupling Effects in Two-Dimensional Electron Systems* (Springer, Berlin, Heidelberg, 2003), pp. 18–20.